

Reducing Impedance at a Li-Metal Anode/Garnet-Type Electrolyte Interface Implementing Chemically Resolvable In Layers

Marius Müller, Johannes Schmiege, Sebastian Dierickx,* Jochen Joos, André Weber, Dagmar Gerthsen, and Ellen Ivers-Tiffée



Cite This: <https://doi.org/10.1021/acsami.1c25257>



Read Online

ACCESS |



Metrics & More



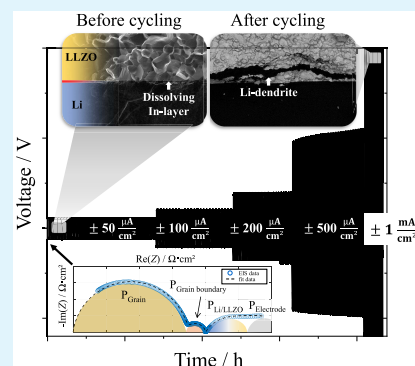
Article Recommendations



Supporting Information

ABSTRACT: Garnet-type $\text{Li}_7\text{La}_3\text{Zr}_2\text{O}_{12}$ (LLZO) is a potential electrolyte material for all-solid-state Li-ion batteries mainly because of its reported excellent chemical stability in contact with Li metal. But good wettability of LLZO and 100% surface coverage of lithium are still a challenge. This study elucidated the suitability of magnetron-sputtered indium in Li(In)/LLZO/Li(In) symmetrical model cells as one of the promising interfacial modifications reported in the literature. Importance was given to the impact of preparation parameters on the surface coverage of Li(In)/LLZO interfaces and the consequences of impedance, cycling stability, and critical current density. SEM and EDXS analyses of In layers of thickness 100 nm to 1 μm revealed complete dissolution of indium in the lithium anode after annealing; 300 nm In layers annealed at 220 °C/10 h provided a surface coverage of >80%, best reproducibility, and a supreme interface resistance R_{int} of 12.4 $\Omega\cdot\text{cm}^2$. Presuming a surface coverage of 100%, an ultimate interface resistance close to 1 $\Omega\cdot\text{cm}^2$ can be expected. The critical current density was determined as 200–500 $\mu\text{A}/\text{cm}^2$ at a charge of 100–250 μAh , whereas 500 $\mu\text{A}/\text{cm}^2$ and above affected cell stability. The increasing voltage plateau was assigned to the increase of the interface resistance R_{int} and the electrolyte resistance $R_{\text{G+GB}}$. SEM, EDXS, and X-ray microtomography analyses after voltage breakdown confirmed Li-dendrite growth along grain boundaries into LLZO, often curved parallel to the interface, indicating short-circuiting of the solid electrolyte. Grain boundary characteristics are supposed to be decisive for lithium deposition in and failure of garnet-type solid electrolytes after cycling.

KEYWORDS: Impedance, electrolyte, X-ray microtomography, garnet-type, electrochemical impedance spectroscopy



1. INTRODUCTION

Solid-state lithium-ion batteries may overcome safety issues in next-generation energy storage systems when a nonflammable solid-state electrolyte (SSE) is used for battery assembly. When combined with a lithium metal anode, even a higher specific energy compared to present material systems can be obtained.

As of today, only a garnet-type $\text{Li}_7\text{La}_3\text{Zr}_2\text{O}_{12}$ (LLZO) has a sufficiently large electrochemical window for withstanding a direct contact with lithium metal foil.^{1,2} However, poor wettability of lithium metal onto untreated LLZO surfaces raises the area-specific interface resistance as high as $\sim 37\,000\ \Omega\cdot\text{cm}^2$ ²³ and the associated limited number of active sites presumably promotes dendrite formation. Remedial actions are reported in the literature, e.g., (i) polishing the LLZO surface itself mechanically,⁴ (ii) using high mechanical pressure for joining thin lithium foils,⁵ (iii) 3D-printing and consecutive sintering of intricate surface architectures,⁶ (iv) replacing pure Li metal by lithium alloy anodes,^{7,8} or (v) introducing a thin layer (Al_2O_3 , ZnO, SiO_2 , Au, Al, Ge, etc.) between lithium metal and LLZO.^{9–14} Improved charge transfer characteristics have also been found for completely clean LLZO surfaces,^{3,15} but require high preparative efforts, i.e., a high-purity and inert atmosphere. In numbers, an isostatic pressure of 400 MPa was

applied to Li/LLZO/Li cells resulting in a negligible interface resistance.⁵ A Li/ $\text{Li}_7\text{La}_{2.75}\text{Ca}_{0.25}\text{Zr}_{1.75}\text{Nb}_{0.25}\text{O}_{12}$ (LLCZN) interface resistance of highly attractive 1 $\Omega\cdot\text{cm}^2$ (based on DC measurements) was reported for an Al_2O_3 interlayer (~ 20 nm) formed by atomic layer deposition (ALD) with excellent cycling stability of symmetrical cells at current densities of 200 $\mu\text{A}/\text{cm}^2$ in ref 9. Similarly, a Li/LLCZN interface resistance of 115 $\Omega\cdot\text{cm}^2$ (based on AC measurements) was realized by evaporation of an ~ 20 nm Ge layer and cycling stability at current densities of 100 $\mu\text{A}/\text{cm}^2$ was demonstrated.¹² Furthermore, a reduction of the Li/LLCZN interface resistance down to $\sim 75\ \Omega\cdot\text{cm}^2$ (based on AC measurements) was achieved by introducing a Li/Al alloy as anode, and the cycling stability of symmetrical Li(Al)/LLCZN/Li(Al) cells was demonstrated at current densities of 200 $\mu\text{A}/\text{cm}^2$.¹⁰ Moreover, an initial interface resistance of 450 $\Omega\cdot\text{cm}^2$ (100 $\Omega\cdot\text{cm}^2$ after reheating) and cycling stability at 100 $\mu\text{A}/\text{cm}^2$

Received: December 31, 2021

Accepted: March 4, 2022

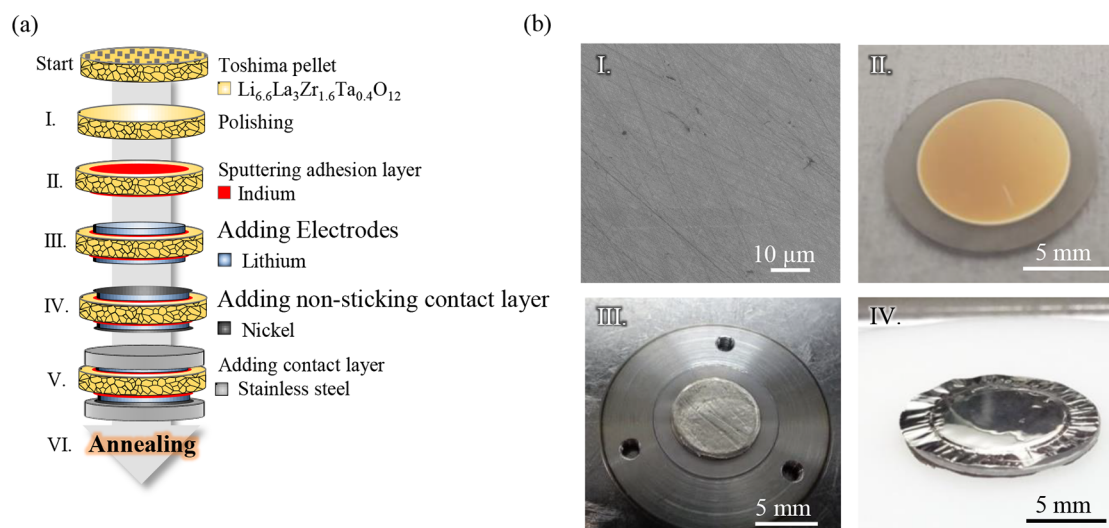


Figure 1. (a) Preparation of symmetrical Li(In)/LLZO/Li(In) cells. (b) SEM image of the polished LLZO surface (step I). Light microscopy image of a 60 s sputtered In layer on LLZO (step II), Li-metal electrode added (step III), and the symmetrically applied Ni foils (step IV).

were reported by utilizing an ~ 30 nm thin ZnO layer.¹³ Last but not least, a silica-based interface modification enabled an interface resistance of $49 \Omega\text{-cm}^2$ and cycling stability at $200 \mu\text{A}/\text{cm}^2$.¹⁴

This work aims for even lower interfacial impedance and better cyclability of a Li(In)/LLZO interface by introducing for the first time a magnetron-sputtered indium layer of thickness 100 nm to $1 \mu\text{m}$. For establishing a reliable preparation routine, we study the influence of a variation in sputter time and annealing temperature. Consequently, the reproducibility of the corresponding interface resistance was examined always on a set of 5 (min) to 15 (max) symmetrical Li(In)/LLZO cells. These experiments seem necessary because indium layers on garnet-based SSE were not yet reported in the literature, while Li(In) alloy anodes were already tested in combination with a sulfide SSE^{16,17} and Lou et al. successfully used indium tin oxide as an interlayer.¹⁸

Numerous studies have already been performed on the interfacial impedance of symmetrical cells with garnet electrolytes.^{4,5,9,10,12,13,19–21} However, at 25°C , none of these studies succeeded in resolving the high-frequency (HF) bulk contribution of LLZO ($f > 10$ MHz) of the impedance spectrum while maintaining the information of the low-frequency (LF) impedance spectrum ($f < 1$ Hz) at the same time. But this distinction is essential, as the different ionic transport processes in solid-state lithium-ion batteries, which contribute to the cell impedance, are distributed over such a wide frequency range. Consequently, two calibrated impedance analyzers (HF and LF) are connected to a framework herein. The activation energies for lithium-ion charge transport in LLZO and for the Li(In)/LLZO interface are determined by temperature-dependent electrochemical impedance spectroscopy (EIS), and, for the first time, charge transport resistance of the grain interior (bulk) and of the grain boundary in LLZO is deconvoluted by the distribution of relaxation times (DRT) using Li(In) reversible electrodes.

The robustness of the Li(In)/LLZO interface under long-term cycling is essential for future applications²² and often quantified by a critical current density (CCD).^{7,11,18} Recently, Flatscher et al. gave a broad overview of measured CCDs¹⁹ ranging between $40 \mu\text{A}/\text{cm}^2$ (their study) and as high as $930 \mu\text{A}/\text{cm}^2$ ²³ for garnet-type (doped) LLZO. Unfortunately, the

listed CCD values cannot be compared easily because of deviating cycling parameters and measurement protocols. Therefore, this work determines CCDs of our best-performing symmetrical Li(In)/LLZO/Li(In) cells for two different test protocols: (i) cycling of the cell with alternating positive and negative current pulses (alternating Li plating and stripping on both electrodes) and (ii) application of unilateral current pulses (Li stripping on one electrode only and plating on the other electrode).

For the Li/LLZO interface in general, two main failure mechanisms were already reported: (i) vacancy accumulation with subsequent contact loss during lithium stripping^{5,24} and (ii) various types of lithium dendrite formation during lithium plating.^{15,25,26} Lithium dendrites were found to propagate into LLZO grains,^{27,28} along grain boundaries,²⁹ and along interconnected pores.^{25,26} Several mechanisms for dendrite formation in LLZO were described in reviews by Krauskopf et al.³⁰ and Cao et al.,³¹ but the underlying electro-chemo-mechanical processes are not yet fully understood. Imaging of lithium dendrites is most frequently performed by optical microscopy^{28,32} and scanning electron microscopy (SEM).^{26,29,32} Both of these techniques are unable to provide a complete analysis since the resolution of optical microscopy is limited, and preparation for SEM is challenging without changing the morphology of the sample surface. In this work, an elaborate preparation method was developed to analyze the Li(In)/LLZO interface after preparation and after long-term cycling. Furthermore, the interface region after passing the cycling experiments is visualized by correlated results from SEM and X-ray microtomography ($\mu\text{-CT}$).

In summary, this work presents a new approach to reliably prepare low-impedance Li(In)/LLZO interfaces. EIS is applied to quantify the impedance contributions in as-prepared Li(In)/LLZO/Li(In) cells and monitor the interface stability during long-term cycling experiments. Results of two different cycling protocols are compared. Morphological analyses by SEM and $\mu\text{-CT}$ are correlated with the electrochemical measurements.

2. EXPERIMENTAL SECTION

2.1. Preparation of Symmetrical Li(In)/LLZO Cells.

Garnet-type structure electrolyte pellets made by Toshiba Manufacturing Co. with

Table 1. Overview of All Preparation Variations of Symmetrical Li(In)/LLZO Cells Throughout This Work^a

cell type	number of prepared cells	DC magnetron sputtering			annealing	
		power (W)	time (s)	layer thickness (nm)	temperature (°C)	time (h)
300_220_2	6	100	300	~1000	220	2
15_220_2	6	100	15	~100	220	2
60_220_2	15	100	60	~300	220	2
60_220_10	5	100	60	~300	220	10
60_250_2	5	100	60	~300	250	2

^aThe sample index stands for “sputtering time_annealing temperature_annealing time”.

the chemical composition $\text{Li}_{6.6}\text{La}_3\text{Zr}_{1.6}\text{Ta}_{0.4}\text{O}_{12}$, a thickness of ~ 500 μm , and a diameter of 16 mm are used in this work. Analysis of as-delivered pellets by scanning electron microscopy (SEM) and X-ray tomography (μ -CT) provides a bulk density higher than 99% and a surface degradation layer with a thickness of 2–3 μm . Energy-dispersive X-ray spectroscopy (EDXS) analysis indicates a double layer with a carbon-enriched outer part and an oxygen-enriched inner part. According to Sharafi et al., these layers consist of Li_2CO_3 and LiOH^3 and originate from exposure to H_2O and CO_2 content in ambient air during and after garnet preparation. Therefore, after pretreatment to pellets, assembly of symmetrical Li(In)/LLZO cells and their characterization by electrochemical impedance spectroscopy (EIS) are performed in an argon atmosphere and described below.

2.1.1. Symmetrically Applied Nonsticking Contact Layer (Ni Foils) to Enable Cell Openings (Step IV). Symmetrical Li(In)/LLZO cells were prepared in a six-step process (see Figure 1a):

- I. Pellets were polished with diamond (Struers DP-Suspension A, 3 and 1 μm), cleaned with 2-propanol, and inspected with a scanning laser microscope (Keyence VK-9710K).
- II. In layers were magnetron-sputtered (vonArdenne CS 730 S) on both pellet sides with a target–substrate distance of ~ 80 mm and a mask with a free aperture of 11.28 mm, delivering indium slightly larger than 1 cm^2 with a reproducible indium content. In this way, the lithium metal foil contacts only with the In-coated region and a Li(In)/LLZO interface is formed with the LLZO. The indium target from vonArdenne was 10 cm in diameter and 2 mm thick. Sputter gas was argon at a flux of 80 sccm, constant pressure of 5×10^{-3} mbar, substrate temperature of 22 °C, and plasma power of 100 W. The sputter time was varied according to Table 1, and the In-layer thickness was quantified by SEM.
- III. Then, In-coated LLZO (see Figure 1, step II) was transferred into an Ar-filled glovebox. Electrodes of 1 cm^2 area and 500 μm thickness from Rockwood lithium foil were symmetrically attached onto the In-coated area.
- IV. In addition, 10 μm nickel foils (nickel 2.4068) were inserted on the top and bottom of lithium electrodes, assuring flawless removal for SEM analysis.
- V. This sandwich was kept between stainless steel current collectors ($d \sim 16$ mm), short-circuiting of the cells while annealing was prevented by a small cavity.
- VI. The final annealing step was made inside a vacuum oven (MBraun VOH-250) at 1 mbar vacuum.

As shown in Table 1, we study in this work 37 symmetrical Li(In)/LLZO cells with three layer thicknesses (100, 300, and 1000 nm), two annealing temperatures (220 and 250 °C), and two annealing times (2 and 10 h). These variations shall disclose the impact of preparation parameters to surface coverage of Li(In)/LLZO interfaces, and the consequences for impedance, cycling stability, and critical current density. Sample denomination (cf. Table 1) refers to sputtering time_annealing temperature_annealing time.

2.2. Electrochemical Characterization. **2.2.1. Cell Testing.** All Li(In)/LLZO cells were tested in a commercial ECC-REF housing with high measurement reproducibility.^{33,34}

The impedance analysis of solid-state lithium-ion batteries with garnet-type electrolytes is challenging as the ionic transport processes are distributed over a frequency range of 10 decades. One HF and one

LF impedance analyzer (for specifications, see Table S1) were operated in the potentiostatic mode as a framework.

The LF range from 50 mHz to 7 MHz is covered with a Biologic VPM-300 multipotentiostat (5 mV amplitude, if not stated otherwise). The HF range from 20 Hz to 120 MHz is recorded with a Keysight E4990A-120 measuring bridge (20 mV). The data quality for $f > 1$ MHz is ensured by calibration measurements, i.e., test fixture compensation performed by measuring under open-circuit, short-circuit, and 50 Ω load resistor conditions. Temperature-dependent calibration is performed with 3 h equilibration time.

The EIS data obtained from the HF and LF measurement devices were combined for analysis in such a way that the last HF data point corresponds to a frequency of 20 Hz and the next LF data point to 18 Hz. The KKT residuals prove the validity of the combined impedance spectra.

Before starting EIS measurements, a consistent initial treatment is applied to all 37 Li(In)/LLZO cell tests. Electrochemical and thermal equilibrium is ensured by a waiting period of 3 h at open-circuit voltage (OCV) at 25 °C. Cell stability is checked by continuous EIS measurements.

In essence, the experiments carried out are classified into three categories: (i) cell reproducibility, (ii) temperature variation, and (iii) cycling stability. Details of the individual test categories are given in the Supporting Information (SI Table S2).

2.2.2. EIS Data Analysis Methods. **2.2.2.1. Distribution of Relaxation Times (DRT).** The analysis of impedance spectra is performed in a multilevel routine, using Matlab-based in-house software. Control of validity and high data quality over the extended frequency range (50 mHz to 120 MHz) is mandatory using the *Kramers–Kronig test* (KKT)³⁵ (available for free download³⁶), followed by a distribution of relaxation times (DRT) calculation.

Any nonscillating electrochemical system can be represented using the DRT approach.³⁷ The separation of electrochemical processes with similar characteristic relaxation time constants by solely analyzing impedance data is sometimes difficult.³⁸ The governing relation between the impedance Z and the DRT is given by³⁹

$$Z(\omega) = R_0 + Z_{\text{pol}}(\omega) = R_0 + R_{\text{pol}} \int_0^{\infty} \frac{g(\tau)}{1 + j\omega\tau} d\tau \quad (1)$$

where $\int_0^{\infty} g(\tau) d\tau = 1$, R_0 is the real part of the impedance when $\omega \rightarrow \infty$, τ is the relaxation time, and R_{pol} is the polarization resistance. The DRT-based analysis of impedance data is well established for fuel cells, conventional lithium-ion batteries, and SSE materials.^{38,40–42} The DRT transforms impedance data into the space of the relaxation times and deconvolutes electrochemical processes with time constants in close proximity. In this work, the DRT analysis was used to preidentify the diverse processes and their characteristic temperature dependencies.

2.2.2.2. Data Fitting. All impedance spectra were fitted using a physically motivated equivalent circuit model. Different RQ elements were used to quantify the impedance contributions. Fitting of the real and imaginary parts (1:1 weight) was performed using a complex, nonlinear, least-square fit (CNLS) routine.

2.2.2.3. Temperature Variation. To determine activation energies $E_{A,i}$ of different electrochemical processes, we use the Arrhenius equation

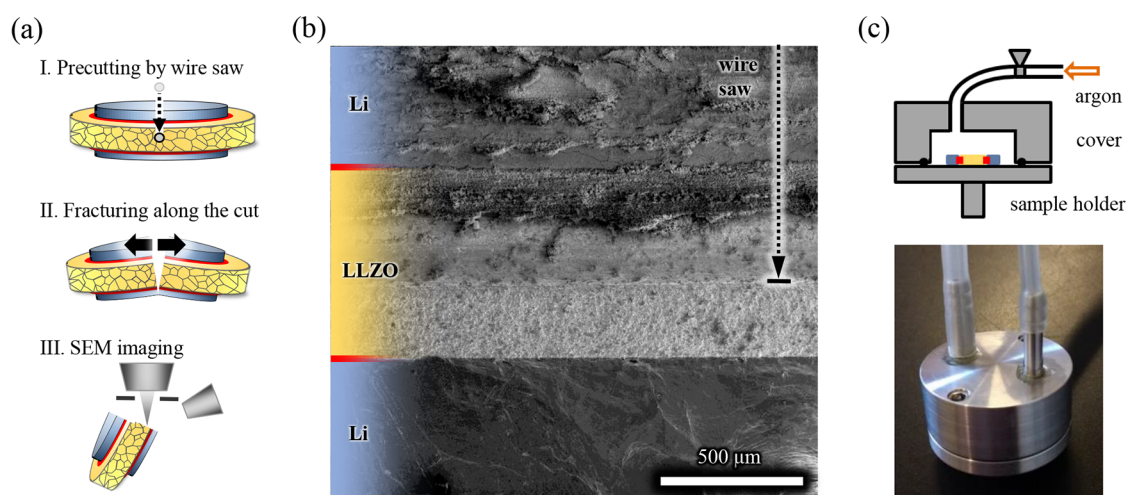


Figure 2. (a) Preparation by wire saw and subsequent fracturing, (b) SE-SEM overview image of the resulting Li(In)/LLZO/Li(In) cross section. The wire saw has cut through the top lithium anode and approximately two-thirds of the LLZO electrolyte. (c) Scheme of the SEM transfer sample holder with a sealed cover to prevent contact with ambient air.

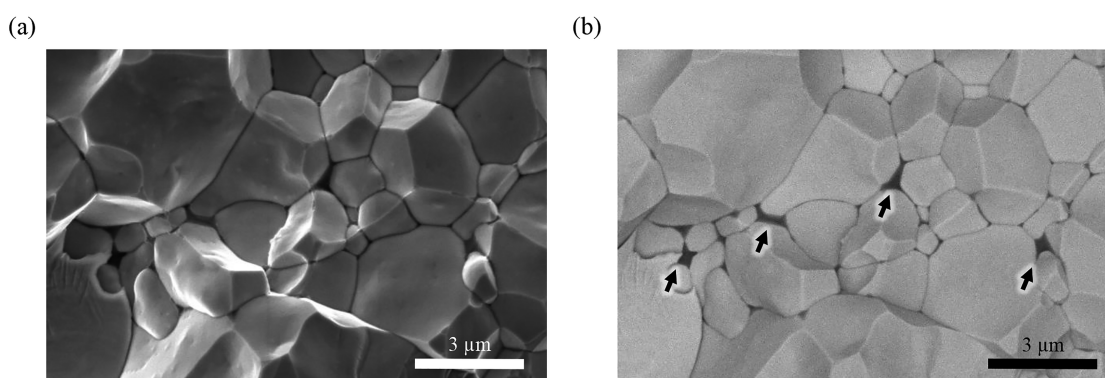


Figure 3. Fracture surface of an LLZO pellet imaged by (a) SE-SEM showing mainly intergranular fracture and (b) material-sensitive BSE-SEM at 5 keV. The dark contrast at grain boundaries (see arrows) indicates the presence of a weakly scattering material such as lithium or lithium compounds.

$$R_i(T) = B \cdot \exp\left(\frac{E_{A,i}}{R \cdot T}\right) \quad (2)$$

where T is the temperature, R_i is the equivalent resistance contribution of the i -th process, B is a preexponential factor, and R is the gas constant.

2.3. Microstructure Analysis by Scanning Electron Microscopy and X-ray Microtomography. Exposure to ambient air must be avoided to prevent the reaction of lithium and LLZO with oxygen, nitrogen (only Li), and water vapor.³ An elaborate preparation procedure for cross-sectional SEM samples of the Li(In)/LLZO interface region was developed in this work.

After electrochemical testing, the *EL-Cell* housing was opened in an inert Ar atmosphere. The stainless steel current collectors and the nickel foils were first removed. A diamond wire saw (Model 3241 with a wire diameter of 0.22 mm, *WELL Diamond Wire Saws SA*, Le Locle, CH) was used to cut a notch through half of the top lithium electrode and partly through the garnet electrolyte, as depicted in [Figure 2a](#).

The cell was then transferred to the glovebox, fractured along the notch under Ar atmosphere, attached on a sample holder using a carbon pad, and transferred into the scanning electron microscope by an airtight and Ar-filled transfer holder (see [Figure 2c](#)). The load-lock of the SEM needs the transfer holder open for a few seconds prior to transfer into the SEM chamber. The newly developed preparation technique yields an uncontaminated fracture cross section of the Li(In)/LLZO interface region. This effect is shown by the low-magnification SEM image in [Figure 2b](#). A notch was cut perpendicular to the upper Li layer and part of the LLZO, and the depth of the wire

saw cut is indicated by the dashed arrow. The SEM contrast of the upper Li layer and LLZO is strongly manipulated by mechanical damage and air exposure. But in the region below, which is the fractured surface, Li and LLZO appear different. Mechanical damage and exposure to ambient air were avoided by a sequence of (i) fracture in Ar atmosphere and (ii) immediate transfer into the scanning microscope.

A Helios G4 FX dual-beam microscope (*Thermo Fisher Scientific*, Waltham) was used for all SEM studies. Secondary-electron (SE-)SEM imaging was performed with the in-chamber ion conversion and electron detector. SEM images with backscattered electrons (BSE) were acquired with the concentric backscatter detector, a solid-state detector that is attached below the objective lens pole piece. BSE-SEM imaging yields material contrast due to the large atomic-number difference between LLZO and lithium. Element distributions were obtained by SEM/EDXS mappings with a primary electron energy of 15 keV. A *Bruker X-Flash 6* system (*Bruker Corporation*, Billerica) implemented in the Helios G4 FX was used for EDXS. However, we note that the Li-K X-ray line with an energy of 55 eV cannot be detected by our EDXS setup. Acquisition and evaluation of EDXS spectra were performed using the *Bruker ESPRIT 2.1* software.

A Xradia Versa 520 X-ray microscope (*Carl Zeiss Microscopy*, Jena) was used for μ -CT analysis. Sample rods with 500 μ m diameter were cut by a diamond wire saw and coated with mounting wax (*Gatan Inc.*, Pleasanton). Imaging was performed with an X-ray source voltage of 140 kV and 700 nm pixel size. The three-dimensional (3D) structure was reconstructed from 3201 projections taken with 0.11° rotation steps between. Shen et al.⁴³ already observed a weak X-ray absorption of

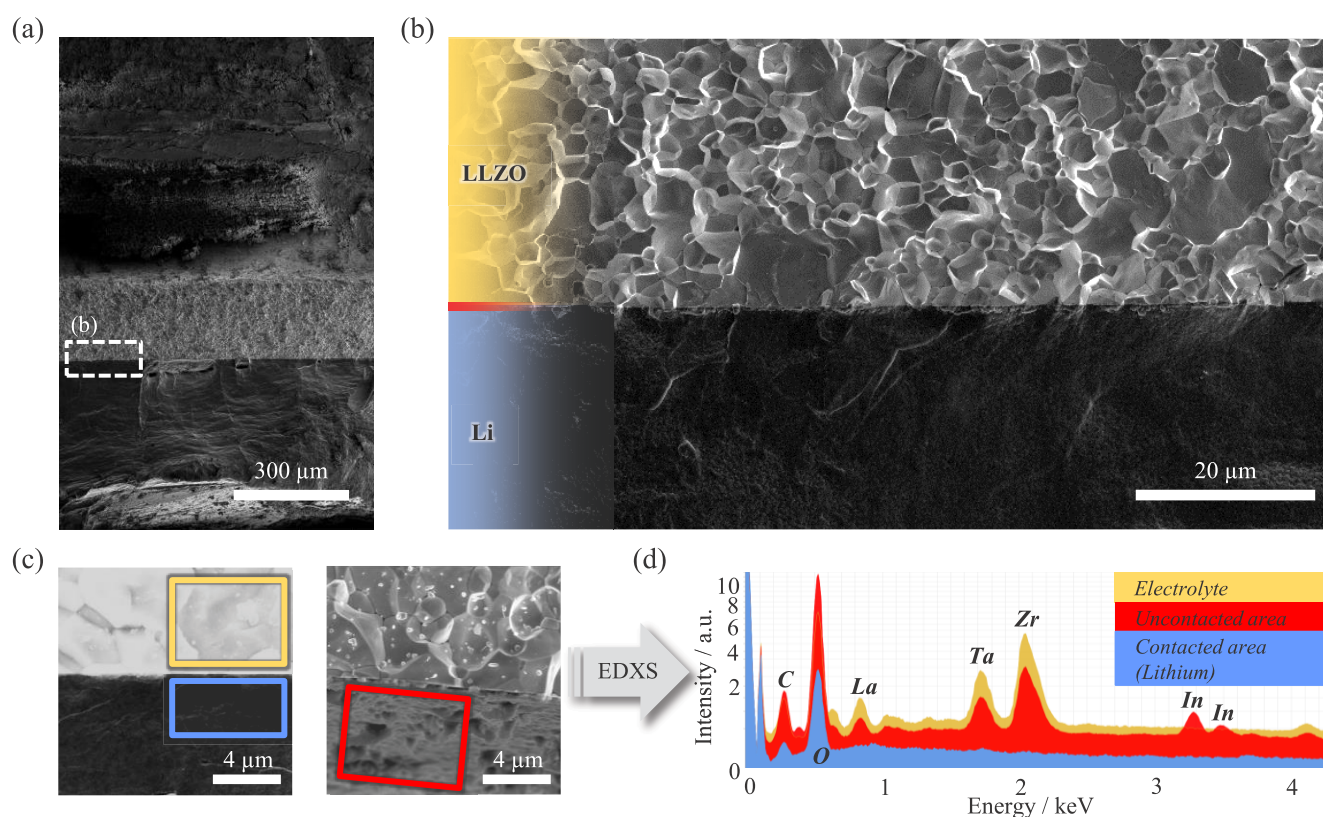


Figure 4. (a) Overview SE-SEM image of a fractured cross section of an as-prepared 60_220_2 cell and (b) SE-SEM image of the contacted interface at higher magnification. (c) SEM images of regions close to the Li(In)/LLZO interface of a 15_220_2 cell that was selected for EDXS analyses. EDXS sum spectra were taken from regions in LLZO electrolyte (yellow), a contacted region close to the interface (blue), and a purposely uncontacted In interlayer (red). The LLZO next to the uncontacted In interlayer shows small lithium particles. (d) Resulting EDXS spectra with square-root intensity scaling where indium X-ray lines at 3.29 keV and 3.49 keV appear only in the uncontacted region.

lithium compared to LLZO, meaning the contrast of empty pores. This phenomenon is shown for our samples in Figure 10a. Image processing and image segmentation of the LLZO and lithium (or pores, respectively) phases were performed with the FEI Avizo 9.2.0 software. This implies noise reduction by a Gaussian filter (3x3x3 voxels kernel) and segmentation of the lithium-rich regions by threshold combined with a black-top-hat filter.

3. RESULTS AND DISCUSSION

3.1. Microstructural Analysis of the Bulk LLZO and the Prepared Li(In)/LLZO Interface. In the SE-SEM image in Figure 3a, the surface topography of a fractured LLZO pellet indicates a preferential fracture along grain boundaries, but occasionally also through the grains. Typical grain diameters are between 1 and 4 μm with an average equivalent diameter of 2.5 μm (cf. grain-size distribution in SI Figure S1b). Material-sensitive BSE-SEM imaging (Figure 3b) of the same sample region with a pronounced dark grain boundary contrast indicates a grain boundary phase containing light elements. Interestingly, this image intensity resembles the intensity of the lithium metal anode (depicted in Figure 4b).

Although the electron-interaction volume for EDXS is much larger than the grain boundary regions, EDXS spectra acquired there show a stronger oxygen signal than the surrounding LLZO grains (Li cannot be detected by EDXS). TEM investigations by Tsai et al.¹¹ revealed a grain boundary phase in their LLZO samples consisting of lithium or lithium oxide. Presumably, both phases also exist at the LLZO grain boundaries of our samples, which were fabricated by Toshiba Manufacturing Co.

Figure 4 depicts the cross-sectional SEM images of the Li(In)/LLZO interface region with an originally 300 nm thick indium layer, after annealing at 220 °C/2 h. Li appears with dark contrast in BSE-SEM and also in SE-SEM images. The lithium anode sticks to the topography of the LLZO grains over almost 1 mm interface length without delamination, which can be seen in Figure 4a and in more detail in Figure 4b. In contrast, lithium anodes with 100 nm thick In layer and same annealing conditions are widely delaminated (see SI Figure S2b), the same for originally 1 μm In layer with a few additional pores (see SI Figure S2c). In general, the In layers themselves are no longer observable in SEM after annealing.

To obtain information on the In distribution, EDXS was performed to analyze the composition of regions in the vicinity of the Li(In)/LLZO interface. EDXS spectra, acquired in the anode at a well-contacted Li interface region (blue frame in Figure 4c), do not show any indium X-ray lines (blue EDXS spectrum in Figure 4d). This indicates that the In content in the vicinity of the Li(In)/LLZO interface must be below the detection limit. Indium X-ray lines were also not detected inside the LLZO (yellow frame in Figure 4c and yellow EDXS spectrum in Figure 4d). Analyzing the LLZO in regions with delaminated Li anode (red frame in Figure 4c) yields X-ray lines for In- $L_{\alpha,\beta}$ at 3.29 and 3.49 keV (red spectrum in Figure 4d). These results verify that the In layer is indeed present after the deposition. Concluding, In diffuses into the Li anode during annealing and results in a very low and probably homogeneous In concentration. With EDXS analysis along the interface region, an indium concentration of 0.2 atom % at the Li(In)/LLZO

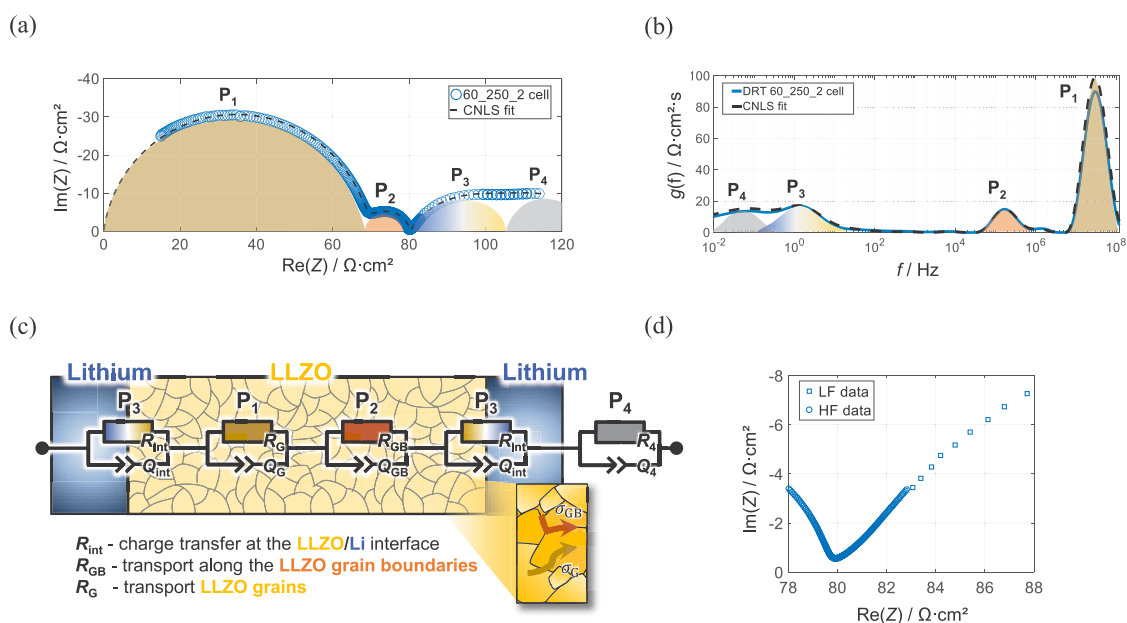


Figure 5. (a) Combined EIS data (blue circles) of a symmetrical Li(In)/LLZO cell from 120 MHz to 50 mHz and the corresponding CNLS-fit (black dashed line) at 25 °C. (b) DRT calculated from impedance data (blue line) and CNLS-fit (black dashed line). (c) Equivalent circuit model for fitting the impedance data (a) consisting of three RQ elements quantifying the resistance contribution R_i and capacity C_i of the grain, the grain boundaries, the Li(In)/LLZO interface, as well as P_4 . (d) Inset of EIS transition from HF (circles) to LF (squares) data.

interface up to 300 μm in the Li anode volume was determined for cells with the thickest In layer (300 s sputtering time corresponding to an In-layer thickness of 1000 nm). Interestingly, this In content agrees with the solubility limit of In in pure Li.⁴⁴ For comparison, a Sn-rich/Al-rich lithium alloy close to the Li/LLZO interface was reported for interlayer of either Sn⁴⁵ or Al.⁷ Our EDXS findings imply a dissolution of indium in lithium as reported for a Mg layer.²¹ This result points to a complete dissolution of all indium layers into the lithium electrode but with a concentration below the EDXS detection limit. However, EDXS was chosen for its ability to deliver the chemical composition of the interface region with spatial solution.

3.2. EIS and Equivalent Circuit Model. **3.2.1. Process Identification, Interface Resistance, and Activation Energy.** The Nyquist diagram in Figure 5a shows the combined HF and LF impedance data of a Li(In)/LLZO/Li(In) cell (60_250_2) with a sputtered In layer of 300 nm. Two slightly overlapping semicircles in the HF range ($f > 10$ kHz) and two apparently overlapping semicircles in the LF range ($f < 100$ Hz) are distinguishable. A direct comparison with EIS data of a Li/LLZO/Li cell without In layer is given in SI Figure S3.

The smooth transition of EIS data between HF (circles) and LF (squares) measurements is proven in Figure 5d. The associated DRT curve in Figure 5b clearly separates two peaks in the HF region with the largest resistance for P_1 at 30 MHz and a smaller resistance for P_2 at 180 kHz and two more peaks with a resistance value comparable to P_2 in the LF region. The characteristic frequency is ~ 1 Hz for P_3 and 10^{-1} – 10^{-2} Hz for P_4 , which is not fully acquired in the measured EIS spectra. Consequently, an equivalent circuit model (ECM) consisting of four RQ elements is proposed (cf. Figure 5c) and the CNLS-fit between 120 MHz and 50 mHz coincides nicely with EIS and DRT experimental data. The corresponding resistances, capacitances, and characteristic frequencies of P_1 , P_2 , and P_3 are shown in Table 2. Although a profound identification of the

Table 2. Quantification of the Resistances, Capacities, Characteristic Frequencies (25 °C), and Activation Energies $E_{A,i}$ for a Symmetrical 60_250_2 Li(In)/LLZO/Li(In) Cell with an Initially 300 nm Thick In Layer^a

process	R_i ($\Omega\text{-cm}^2$)	f_i (Hz)	C_i (F)	$E_{A,i}$ (eV)	published $E_{A,i}$ (eV)
(P_1) grain	69	3.0×10^7	9.6×10^{-11}	0.40	0.37 ⁴⁶ – 0.41 ^{47**}
(P_2) grain boundary	10.9	180×10^3	6.8×10^{-8}	0.45	0.46 ^{***,5} 0.44 ^{***,48}
(P_3) Li(In)/LLZO-interface	12.4	1.4	9.2×10^{-3}	0.52	0.37 ⁵

^aThe activation energies, obtained from impedance data in Figure 6b, are compared with recently published literature values for LLZO with 0.4 stoichiometric tantalum content (* for 0.3 stoichiometric Ta content, ** for 0.375 stoichiometric Ta content, *** LLZO with 0.25 stoichiometric Al content since no values are reported for Ta-substituted LLZO).

nature of P_4 is not possible yet, the nature of the three processes P_1 , P_2 , and P_3 are highlighted by EIS measurements at different temperatures (10, 15, 20, 25, 30, 40, and 50 °C). EIS data, the corresponding DRTs, and evaluation of the activation energies are shown in Figure 6a–c, respectively.

As expected, the total impedance contribution of the Li(In)/LLZO/Li(In) cell shrinks in the HF and in the LF range with increasing temperature, but only the DRT allows both division and quantification of the HF contributions P_1 and P_2 . Using the in-house developed fitting routine and the 4 RQ-ECM, the values for resistance, capacitance, and activation energy $E_{A,i}$ for P_1 , P_2 , and P_3 are now calculated, summarized, and compared with recent publications in Table 2.

The activation energy of the dominant HF process P_1 is 0.40 eV and coincides with previously published data correlated with the ion transport in the LLZO grain interior (often referred to as

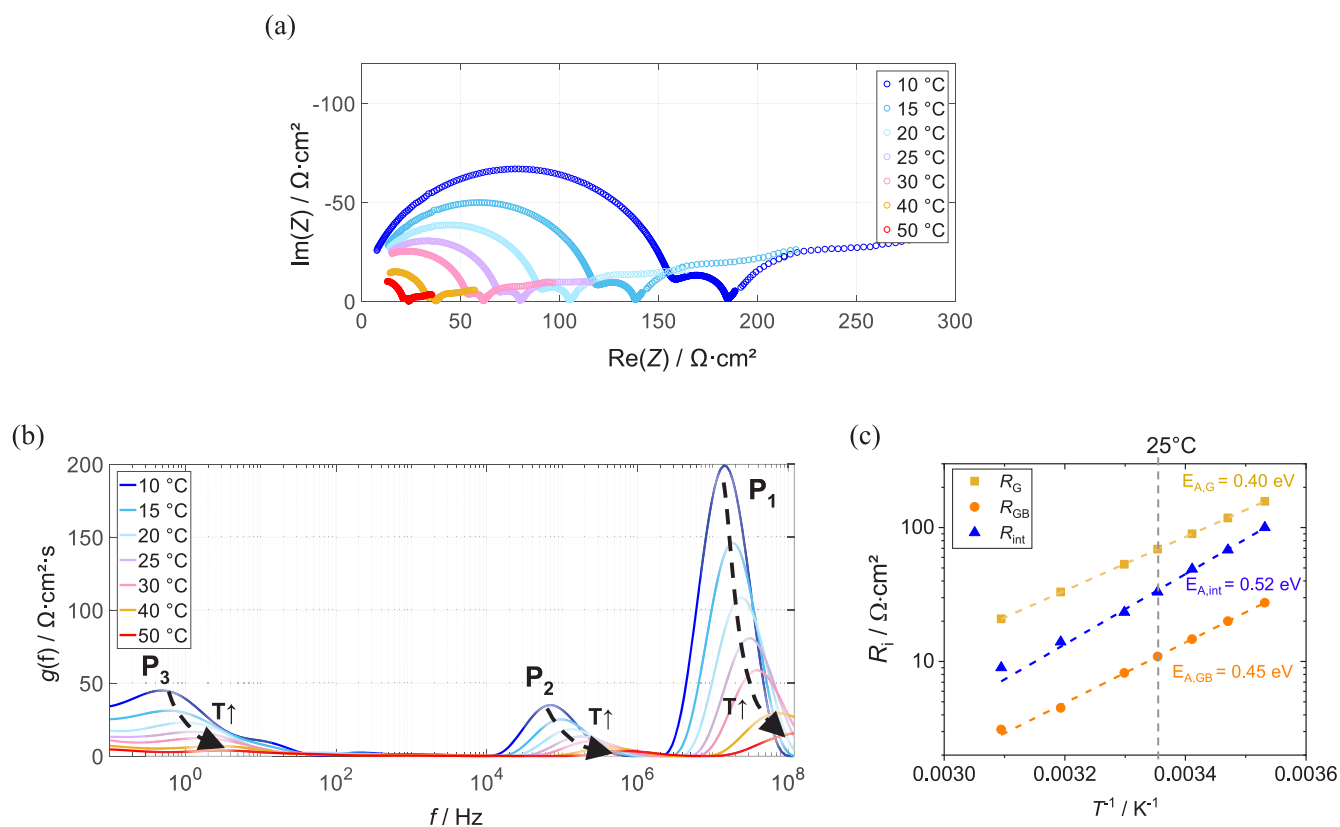


Figure 6. (a) EIS data of a 60_250_2 cell measured for different temperatures and (b) corresponding DRT data. Activation energies for grain, grain boundary, and the Li(In)/LLZO interface are calculated from an Arrhenius plot in (c). All fits exhibit a reduced chi-square value above 0.998.

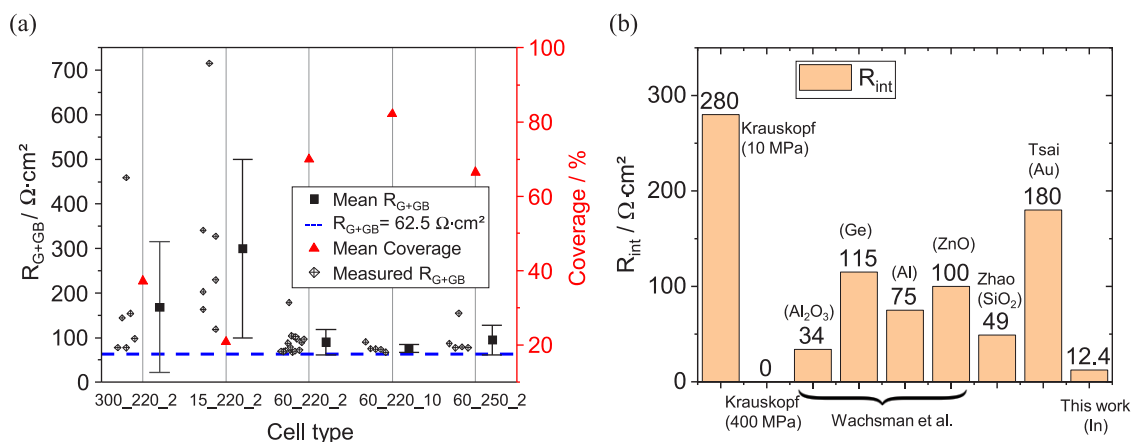


Figure 7. (a) Summary of the total ionic resistance R_{G+GB} at 25 °C and the surface coverage of symmetrical cells obtained from parameter variations of In-layer thickness, annealing time, and temperature. The best coverage is achieved for cells of type 60_220_10 followed by 60_250_2 and 60_220_2 cells. All data were normalized with respect to a representative pellet thickness of 500 μm . (b) Comparison of the measured interface resistance at 25 °C with other publications (AC measurements only).

bulk transport) with 0.3 (0.4 in this work) stoichiometric tantalum content. The characteristic frequency $f_{G,\text{char}} = 3.0 \times 10^7$ Hz corresponds well to HF-EIS data published by Sakamoto et al. for the bulk charge transport in Al-substituted LLZO ($\text{Li}_{6.28}\text{Al}_{0.24}\text{La}_3\text{Zr}_2\text{O}_{12}$).⁴⁸ Hence, the dominant HF process P_1 is assigned to Li-ion charge transport through LLZO grains. The smaller semicircle P_2 in Figure 5a with a characteristic frequency of 1.8×10^5 Hz shows a slightly higher activation energy of 0.45 eV and a comparable temperature dependence. We assign P_2 to the supplementary grain boundary charge transport, which is

thereby evaluated and published for the first time for tantalum-substituted LLZO. However, Krauskopf et al.⁵ reported 0.46 eV and Sakamoto et al.⁴⁸ 0.44 eV for grain boundary charge transport within aluminum-doped LLZO. In a theoretical study by Yu et al.,⁴⁹ the activation energy for grain boundary transport is up to $\sim 35\%$ higher than for bulk LLZO. For comparison, own measurements on undoped $\text{Li}_{0.29}\text{La}_{0.57}\text{TiO}_3$ (LLTO) show significantly lower $E_{A,G}$ of 0.31 eV for transport through the grains (bulk) and $E_{A,GB}$ of 0.36 eV for ion transport along the grain boundaries,³⁸ differing by $\sim 20\%$ in our case.

Table 3. Comparison of Interface Preparations, Characteristic Frequencies, and Capacitances at 25 °C of Li(In)/LLZO Interfaces Reported in the Literature

publication	interface preparation	f_{int} (Hz)	C_{int} (F·cm ⁻²)	R_{int} (Ω·cm ²)
Krauskopf et al. ⁵	10 MPa pressure at the counter electrode	~ 2500 ^a	~2 × 10 ⁻⁷	280 ^a
Krauskopf et al. ⁵	400 MPa pressure at the counter electrode	~ 2500 ^a	~0.5 × 10 ⁻⁷	0
Wachsman et al. ⁹	5–6 nm Al ₂ O ₃ interlayer; 1 h at 250 °C annealing			34
Wachsman et al. ¹²	20 nm Ge layer; 10 min at 200 °C annealing			115
Wachsman et al. ¹³	30 nm ZnO layer; 30 min at 300 °C annealing (before 30 min at 230 °C)			100
Zhao et al. ¹⁴	20 nm Au layer; 2 h at 200 °C annealing;			49
Tsai et al. ¹¹	10 nm SiO ₂ layer; 5 h at 100 °C annealing; 0.1 MPa pressure	~200 ^b	4.3 μF	180 ^a
this work	300 nm In layer	1.4	9.2 × 10 ⁻³	12.4

^aThe values were estimated from the correspondent publication. ^bCalculated values.

P_3 with a characteristic frequency of 1.4 Hz, superimposed by the (physically not elucidated but in the fitting-procedure considered) P_4 , has an activation energy of 0.52 eV and a significantly higher temperature dependence and is allocated to the transport of Li ions across the Li(In)/LLZO interface. Consequently, the impedance of a single Li(In)/LLZO interface is as low as 12.4 Ω·cm² with a capacitance of 9.2 mF for the herein discussed symmetrical Li(In)/LLZO/Li(In) cell type (60_250_2). Evidently, our combined EIS & DRT analysis disclose both grain and grain boundary contributions in LLZO and such a small interfacial resistance measured at a spring load pressure of 0.1 MPa. Krauskopf et al. utilized a symmetrical Li/LLZO/Li cell under high pressures (~400 MPa) when they reported negligibly small charge transfer kinetics and assumed an interface resistance originating from current constriction inside LLZO. Interestingly enough, the interface resistance reported by Krauskopf would be as high as ~500 Ω·cm² when extrapolated to an isostatic pressure of 0.1 MPa, and hence, the constriction theory in ref 5 is not applicable to our experimental results. As the symmetrical cells exhibited no intercalation-type electrodes, a Warburg-type diffusion impedance related to Li diffusion in the active material has to be excluded. Furthermore, we expect no impedance contribution of lithium diffusion through the originally 300 nm thick In layer, as EDXS analysis proved the chemical dissolution of the 300 nm In layer after annealing at 220 °C/10 h in the entire Li-metal electrode (see Section 3.1).

Consequently, P_1 , P_2 , and P_3 are associated with the ion transport inside the grains, ion transport across the grain boundaries, and charge transfer across the Li(In)/LLZO interface, respectively, as indicated in the ECM in Figure 5c. The origin of the smallest process P_4 has to be further investigated, i.e., by impedance measurements in the μHz range as well as time-domain measurements. Published Li/LLZO interface resistances with permanent metal/metal oxide interlayers (Ge, Au, Al₂O₃, ZnO, SiO₂), determined by AC-based measurements, are depicted in Figure 7b and in Table 3. Utilizing various interlayers, the group of Wachsman reports 34 Ω·cm² (Al₂O₃), whereas other configurations and groups are ~2 to 5 times higher.

3.2.2. Variance of the Li(In)/LLZO Interface Resistance. The variance of Li(In)/LLZO interfacial quality, prepared with different In-layer thicknesses and at different annealing temperatures, is now assessed. For this purpose, surface coverage is determined by comparing the theoretical resistance $R_{\text{G+GB,theo}}$ and the measured resistance $R_{\text{G+GB,meas}}$. $R_{\text{G+GB,theo}}$ for a plain pellet is directly linked to the ionic charge transport σ_{ion} , the surface area A_{pellet} and the thickness d_{pellet}

$$R_{\text{G+GB,theo}} = \frac{1}{\sigma_{\text{ion}}} \cdot \frac{d_{\text{pellet}}}{A_{\text{pellet}}} \quad (3)$$

The ionic conductivity σ_{ion} was determined by EIS measurements of symmetrical Ni/LLZO cells with blocking nickel electrodes (cf. SI Figure S4). With $d_{\text{pellet}} = 500 \mu\text{m}$, $A_{\text{pellet}} = 1 \text{ cm}^2$, and $\sigma_{\text{ion}} = 8 \times 10^{-4} \text{ S/cm}$ at 25 °C, the resistance $R_{\text{G+GB,theo}}$ results in 62.5 Ω. This value is equivalent to a symmetrical Li(In)/LLZO cell when 100% of its surface is covered with lithium. When the pore size d_{pore} of pores, originating from uncontacted surface regions at the interface, is small compared to d_{pellet} (i.e., $d_{\text{pore}} \ll d_{\text{pellet}}$), the active surface area A_{active} can be determined from the measured resistance as follows

$$A_{\text{active}} = \frac{1}{\sigma_{\text{ion}}} \cdot \frac{d_{\text{pellet}}}{R_{\text{G+GB,meas}}} \quad (4)$$

The coverage rate α_{eff} is obtained from comparison of the measured resistance $R_{\text{G+GB,meas}}$ and the theoretical resistance $R_{\text{G+GB,theo}}$ for a fully covered interface

$$\alpha_{\text{eff}} = \frac{A_{\text{active}}}{A_{\text{pellet}}} = \frac{R_{\text{G+GB,theo}}}{R_{\text{G+GB,meas}}} \times 100 \% \quad (5)$$

Table 4 and Figure 7a display the electrolyte resistance $R_{\text{G+GB}}$, its standard deviation, and the coverage rate α_{eff} of Li(In)/LLZO interface evaluated for different annealing parameters.

Table 4. Electrolyte Resistance $R_{\text{G+GB}}$, Standard Deviation, and Coverage of Li(In)/LLZO Interface Evaluated for Different Annealing Parameters of a 300 nm Thick In Layer^a

cell type	mean $R_{\text{G+GB}}$ (Ω·cm ²)	standard deviation (Ω·cm ²)	coverage α_{eff} (%)
60_220_2	89	27	70
60_220_10	76	9	82
60_250_2	95	30	66

^aThe increase of the coverage demonstrates the sensitivity to the annealing parameters.

The highest surface coverage is reached with 82% for cells with an originally 300 nm thick In layer after annealing at 220 °C for 10 h, corresponding to an $R_{\text{G+GB}}$ of 76 Ω·cm² with a small standard deviation of 9 Ω·cm². Changing either annealing time (2 h) or annealing temperature (250 °C) for a 300 nm thick In layer increases the value for $R_{\text{G+GB}}$ by 20–30%, triples the standard deviation, and lowers the mean surface coverage to 70% and 66%, respectively. Changing the In-layer thickness from 300 to 100 nm resulted in a rapid decline of the surface coverage to only 20%, indicated by rising values for $R_{\text{G+GB}}$ and its

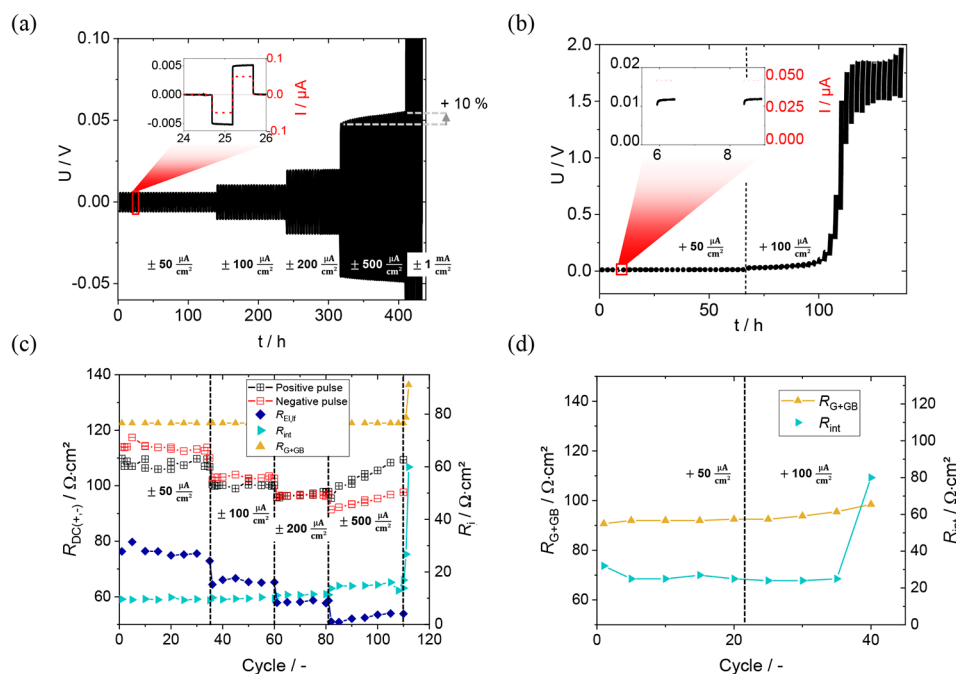


Figure 8. Results of long-term cycling experiments of symmetrical cells at 25 °C. In symmetric cycling experiments according to the CCD protocol I ((a) and (c)), the critical current density is determined between 200 and 500 $\mu\text{A}/\text{cm}^2$ (with respect to 1 cm^2 geometrical contact area). The interface resistance R_{int} increases slowly at 500 $\mu\text{A}/\text{cm}^2$ and significantly at 1 mA/cm^2 . The DC resistances of $R_{\text{Ei,LF}}$ as well as positive and negative pulses $R_{\text{DC}(+,-)}$ increase when increasing the current density to 500 $\mu\text{A}/\text{cm}^2$. For the CCD protocol II (plating and stripping only experiment), the voltage plateaus increase strongly when increasing the current density to 100 $\mu\text{A}/\text{cm}^2$ (b).

standard deviation. The same outcome is valid for increasing the layer thickness from 300 nm to 1 μm , when the surface coverage dropped to 40%. As a consequence, in layers below 100 nm and above 1 μm were not investigated. Preliminary studies without In layers delivered a performance of inferior quality, and the corresponding measurements are summarized in Supporting Information Figure S3. The above findings point to the effectiveness of the investigated fabrication parameters on the quality of the Li(In)/LLZO interface. While the sputtering time at a constant power governs the indium-layer thickness, annealing temperature combined with annealing time settles the surface coverage and interfacial resistance. In the anticipation of the following experiments, 300 nm In layers annealed at 220 °C/10 h provided the highest surface coverage, best reproducibility, and lowest interfacial resistance (see Figure 7a, Table 4).

We are rather confident, that the surface coverage can be increased to nearly 100% when the preparation routine of symmetrical Li(In)/LLZO/Li(In) cell type (60_220_10) is fine-tuned and transferred to a more robust preparation at a technical scale. In this case, an interface resistance closer to 1 $\Omega\cdot\text{cm}^2$ can be expected. This highly attractive value, till now based on DC measurements only, has been reported for the first time by the group of Wachsman⁹ for an ALD-deposited Al_2O_3 interlayer (~ 20 nm). To date, other metals such as germanium (~ 20 nm)¹² and gold (20 nm)¹¹ were used for symmetrical Li(buffer-metal)/LLZO cell assembly but resulted in much higher interface resistances (see Figure 7b).

3.2.3. Cycling Stability and Critical Current Density. The cycling stability and CCD⁵⁰ are analyzed in this section, as they are important for the application of a solid electrolyte in a lithium-ion cell. In today's lithium-ion batteries with liquid electrolytes, current densities typically range from 1 to 25 mA/

cm^2 .⁵¹ Symmetrical cells with the lowest interface resistances were long-term cycled at 25 °C applying the (i) CCD protocol I (plating and stripping on both Li electrodes) and (ii) CCD protocol II (see SI Table S2). In symmetric cycling experiments (Figure 8a,c), the critical current density is reached between 200 and 500 $\mu\text{A}/\text{cm}^2$ (with respect to 1 cm^2 geometrical contact area), and the interface resistance R_{int} increases slowly at 500 $\mu\text{A}/\text{cm}^2$ and significantly at 1 mA/cm^2 . The temporal evolution of the measured impedance spectra of both CCD protocols is shown in SI Figure S5.

The total positive and negative DC resistances for the symmetrical cell $R_{\text{DC}(+,-)} = U(t = 30 \text{ min})/j_{(+,-)}$ are calculated using voltage U and current density values j of positive and negative pulses measured 30 min after the load. Using this value, a resistance contribution $R_{\text{Ei,LF}}$ representing the LF process P_4 for both electrodes can be calculated

$$R_{\text{Ei,LF}} = R_{\text{DC}(-)} - R_{\text{G+GB,meas}} - R_{\text{int}} \quad (6)$$

The DC resistances of $R_{\text{Ei,LF}}$ as well as positive and negative pulses $R_{\text{DC}(+,-)}$ increase when increasing the current density to 500 $\mu\text{A}/\text{cm}^2$.

$R_{\text{Ei,LF}}$ and R_{DC} depend on the applied current density since their contributions decrease in a stepwise manner with increasing current density up to 200 $\mu\text{A}/\text{cm}^2$ (cf. Figure 8c). However, increasing the current density to 500 $\mu\text{A}/\text{cm}^2$ leads to cell instability by means of an increasing voltage plateau. The voltage increase can clearly be assigned to the increase of the interface resistance R_{int} (turquoise symbols in Figure 8c,d) and $R_{\text{Ei,LF}}$ (blue symbols in Figure 8c), while the total ionic resistance $R_{\text{G+GB}}$ (yellow symbols in Figure 8c,d) does not increase significantly. Thus, the critical current density for symmetrical cycling lies between 200 and 500 $\mu\text{A}/\text{cm}^2$. Table 5 compares this work's results with literature values, i.e., CCDs and the

Table 5. Literature Overview and Comparison of Symmetrical Model Cells with Different Interlayers, with respect to the Maximum Current Densities Obtained Over Several Hours of Stable Cycling (Comparable to CCD Protocol I)

publication	interlayer	CCD ($\mu\text{A}/\text{cm}^2$)	stripped lithium p. cycle (μm)	charge p. cycle (μAh)
Wachsman et al. ⁹	Al_2O_3	200	0.5	100
Wachsman et al. ¹²	Ge	<100	<0.25	<50
Wachsman et al. ¹³	ZnO	100	0.15	~30
Wachsman et al. ¹⁰	Al	200	0.09	~17
Zhao et al.	SiO_2	200	1	200
Guillon et al. ¹¹	Au	80	0.8	160
He et al. ⁴⁵	Sn	500	1.25	250
this work	In	200–500	0.5–1.25	100–250

equivalent lithium amount stripped or plated (calculated using the measured charge per cycle and the specific capacity of Li) per cycle of symmetric cells prepared with different permanent interlayers.

The Li(In)/LLZO/Li(In) cells developed in this work outperform by far (Au, Ge in refs 11, 12) or match (Al_2O_3 in ref 9) the performance of permanent metal layer-based cells.

The behavior at even higher current densities was evaluated also for CCD protocol I. An increase to $1 \text{ mA}/\text{cm}^2$ leads to a strong increase of the resistances R_{int} and $R_{\text{G+GB}}$ and to a voltage breakdown. This indicates a geometrical contact loss of the stripped electrode and the propagation of lithium dendrites into the LLZO (cf. Section 3.3). As mentioned in the Introduction section, there is no common standard or measurement protocol established in terms of critical current density determination under long-term cell operating conditions. Often a protocol is applied to determine the CCD, in which an increasingly positive and negative DC current is alternately applied as a single step. Since each current density is typically applied only *once*, the measured CCD might be overestimated.

In a similar manner, the critical current density for CCD protocol II of lithium ions was determined. In Figure 8b (inset), the resulting voltage plateaus at a current density of $50 \mu\text{A}/\text{cm}^2$ are stable over a long period of time. However, when the current density is doubled, the voltage plateaus become unstable and increase strongly above 1.5 V. The voltage increase can be correlated with an (i) electrolyte and (ii) interface resistance increase resulting in partial contact loss due to the stripping and plating of a total of $6.6 \mu\text{m}$ lithium (with respect to the $500 \mu\text{m}$ thick metal electrode) within the first 100 h. Thus, we conclude

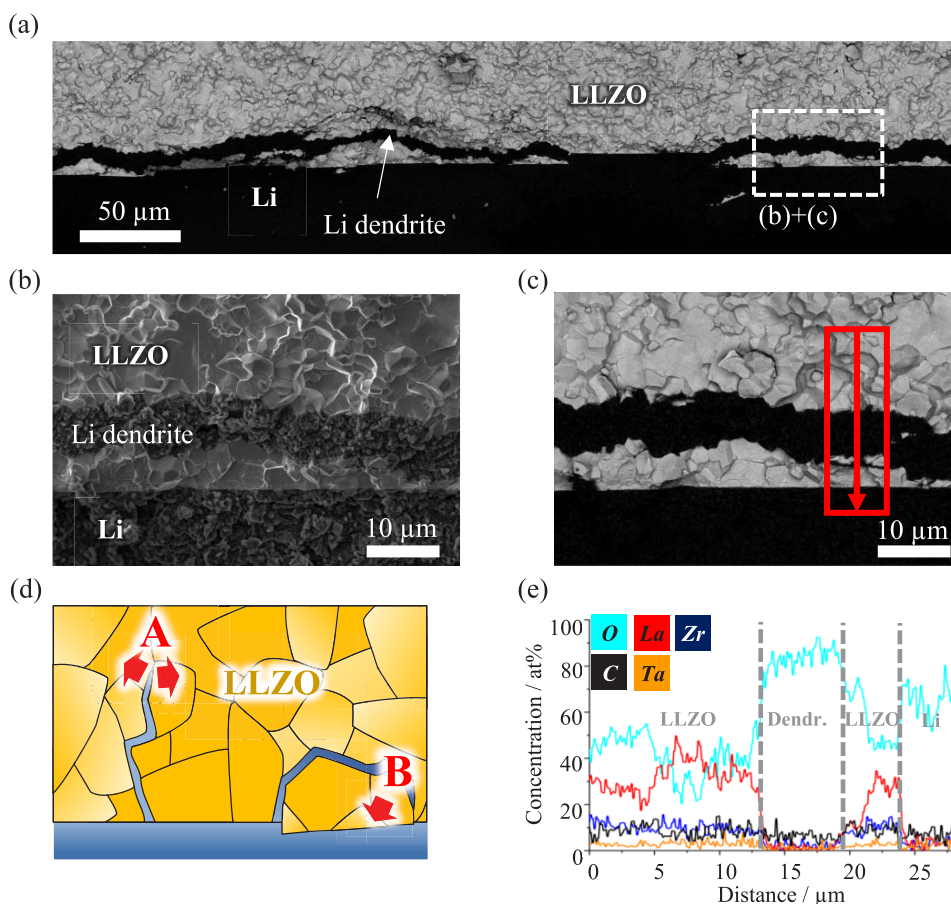


Figure 9. Investigation of dendrites by SEM. (a) 5 keV BSE-SEM overview image of a large Li dendrite in the LLZO electrolyte. (b) SE-SEM and (c) BSE-SEM image of the interface region marked by the frame in (a). (d) Scheme of different dendrite growth morphologies. (e) Quantified EDXS line scan of the O, La, Zr, C, and Ta concentrations acquired across the Li(In)/LLZO interface marked in (c) by a red frame. The lithium content is not included in the quantification.

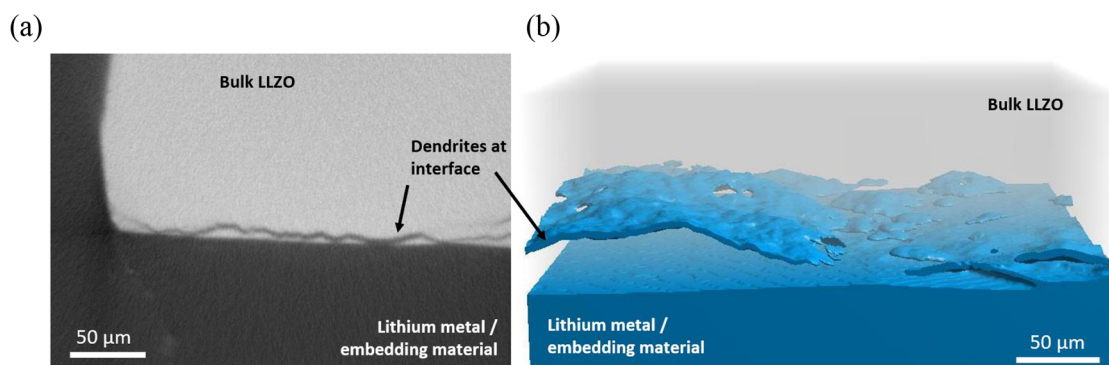


Figure 10. Postmortem X-ray microtomography (μ -CT) imaging. (a) Example image from μ -CT showing disconnected LLZO segments at the interface. (b) 3D rendering of a segmented μ -CT reconstruction at the Li(In)/LLZO interface. Lithium metal is shown in blue, and LLZO is transparent to visualize the interface and dendrite morphology.

that the critical current density for asymmetric CCD protocol II of Li lies between 50 and 100 $\mu\text{A}/\text{cm}^2$ for our cells. These results are in good accordance with the experimental and theoretical study of Krauskopf et al.⁵ Based on the vacancy relaxation model suggested by Schmalzried et al.,⁵² a critical current density between 50 and 200 $\mu\text{A}/\text{cm}^2$ was proposed under which the interface (at room temperature and no applied pressure) will remain morphologically stable.⁵ In a long-term stripping experiment, they reported complete contact loss after lithium dissolution of 5.8 μm thickness, almost confirming our measurements.⁵ The results of our work confirm that the Li(In)/LLZO interface cannot be loaded with technically relevant areal capacities as high as 5 mAh without high external mechanical load.⁵³

3.3. Postmortem Analysis by μ -CT and SEM. After the symmetrical plating and stripping experiments (CCD protocol I) to a maximum current density of 1 mA/cm^2 of the symmetric Li(In)/LLZO/Li(In) cells with a 300 nm thick In layer (annealing at 220 $^\circ\text{C}$ for 10 h), an extensive postmortem analysis by SEM and μ -CT was performed.

Figure 9a shows a material-sensitive BSE-SEM image exhibiting large Li dendrites that originate at the Li(In)/LLZO interface and penetrate the LLZO electrolyte up to a distance of 70 μm from the interface (cf. Supporting Information Figure S6a).

The dendrites grow predominantly parallel to the interface and along grain boundaries (cf. more detailed SEM image in SI Figure S3b). Higher-magnification BSE- and SE-SEM images of the same Li(In)/LLZO interface region are shown in Figure 9b,c. The topography image in Figure 9b reveals the fine-grained lithium structure and trans- and intergranular fracture in the LLZO electrolyte. The quantified EDXS line scan (Figure 9e), acquired in the region indicated by the red arrow in Figure 9c, shows only an oxygen signal in the regions of the lithium anode and the dendrite (apart from a small carbon content) because Li cannot be detected by EDXS. The oxygen signal can be attributed to oxidation by the short air exposure during sample transfer into the electron microscope. Contamination of the sample in the microscope is the origin of the small carbon content. The nominal composition of our LLZO pellets is 71 atom % oxygen, 18 atom % lanthanum, 9 atom % zirconium, and 2 atom % tantalum (excluding lithium in the analysis). While EDXS measurements from polished bulk LLZO samples (not shown here) yield the nominal composition, the element concentrations of the quantified line scan (Figure 9e) show

deviations, which are assigned to an artifact of EDXS analyses from nonplanar surfaces.

Figure 10 shows μ -CT results of a Li(In)/LLZO interface region in a cell with the same preparation and cycling parameters as in Figure 9.

An example image from the reconstructed image stack reveals a large dendrite close to the Li(In)/LLZO interface (Figure 10a), with a high image intensity representing stronger X-ray absorption in LLZO and dark contrast for Li and the protective coating. Figure 10b shows the dendrite after 3D reconstruction of the image stack and segmentation of the Li phase (blue color). Consistent with the SEM images in Figure 9, the Li dendrite grows parallel to the Li(In)/LLZO interface. μ -CT imaging and reconstruction are only possible for Li dendrites with a thickness of more than 1 μm , but complementary SEM images suggest that large lithium dendrites are connected by smaller lithium dendrites.

The origin of dendrite formation has been extensively investigated in the recent past and was summarized already in review papers (Krauskopf et al.⁵ and Cao et al.³¹). Several groups suggest (e.g., Dong et al.⁵⁴ and Han et al.⁵⁵) that the high electronic conductivity of LLZO in combination with a local overshoot of the chemical potential of Li^+ causes dendrite formation. As a consequence, dendrite formation is expected not only in the vicinity of the Li(In)/LLZO interface but also further inside the solid electrolyte. But in this study, a large-volume analysis by μ -CT on highly cycled cells confirmed the existence of lithium dendrites only up to a distance of 20–50 μm to the interface region. However, as this finding always depends on the resolution of the applied technique, the existence of minor dendrites within LLZO is not excluded. A remarkable observation, only achievable by three-dimensional tomography, is the in-parallel growth of dendrites along the Li(In)/LLZO interface. It seems reasonable that the electronic properties are not the solitary factor influencing dendrite formation and dendrite growth. The mechanical properties may also play a role as illustrated in Figure 9d, as lithium accumulation in dendrites causes a local volume expansion.⁵⁶ For dendrite growth perpendicular to the Li(In)/LLZO interface (mechanism A in Figure 9d), the force exerted by the high elastic modulus of LLZO (150 GPa)⁵⁷ acts against Li propagation. A reduced mechanical force is expected close to the Li(In)/LLZO interface. In this region, fragmented LLZO parts can be pressed into the soft Li electrode (mechanism B in Figure 9d). Large LLZO fragments of several 100 μm , disconnected from the solid

electrolyte (“spalling-type” lithium penetration), were also observed by Kazyak et al.³²

4. CONCLUSIONS

A low interface resistance between a lithium metal anode and a $\text{Li}_7\text{La}_3\text{Zr}_2\text{O}_{12}$ (LLZO) solid electrolyte and its high long-term cycling stability are of great consequence for all-solid-state lithium batteries. This study elucidated the suitability of magnetron-sputtered indium in $\text{Li}(\text{In})/\text{LLZO}/\text{Li}(\text{In})$ symmetrical model cells as one of the promising interfacial modifications reported in the literature. Importance was given to the impact of preparation parameters on the surface coverage of $\text{Li}(\text{In})/\text{LLZO}$ interfaces and the consequences of impedance, cycling stability, and critical current density.

- SEM and EDXS analyses of In layers of thickness 100 nm to 1 μm revealed complete dissolution of indium in the lithium anode after annealing.
- 300 nm In layers annealed at 220 $^\circ\text{C}/10$ h provided a surface coverage of >80%, and best reproducible and smallest impedance values. The ultimate interface resistance R_{int} of 12.4 $\Omega\text{-cm}^2$ was reported for the first time by impedance measurements and achieved in a test configuration without exterior mechanical force.
- It is presumed that the surface coverage can be increased to nearly 100% when the preparation routine is fine-tuned and transferred to a technical scale. In this case, an interface resistance close to 1 $\Omega\text{-cm}^2$ can be expected. This highly attractive value, based on DC measurements, was reported by the group of Wachsman for an ALD-deposited Al_2O_3 layer (~ 20 nm).
- Using two testing protocols, the critical current density was determined as (i) 200–500 $\mu\text{A}/\text{cm}^2$ at a charge of 100–250 μAh and (ii) 50–100 $\mu\text{A}/\text{cm}^2$ agreeing with published theoretical calculations and outperforming Au and Ge interlayers.
- Current densities of 500 $\mu\text{A}/\text{cm}^2$ and above affected cell stability. The increasing voltage plateau was assigned to the increase of the interface resistance R_{int} and the electrolyte resistance $R_{\text{G+GB}}$.
- Postmortem analysis by $\mu\text{-CT}$ and SEM after voltage breakdown indicated short-circuiting of the solid electrolyte. Li dendrites were observed growing along LLZO grain boundaries, preferentially curving parallel to the $\text{Li}(\text{In})/\text{LLZO}$ interface after some 20–50 μm . Grain boundary characteristics are supposed to be decisive for lithium deposition in and failure of garnet-type solid electrolytes after cycling.

■ ASSOCIATED CONTENT

SI Supporting Information

The Supporting Information is available free of charge at <https://pubs.acs.org/doi/10.1021/acsami.1c25257>.

Grain-size distribution; SEM images of as-prepared and cycled cells; EIS data of $\text{Ni}/\text{LLZO}/\text{Ni}$ cells; EIS data of $\text{Li}/\text{LLZO}/\text{Li}$ cells; EIS data of cycled cells; measurement device specifications; and measurement protocols (PDF)

■ AUTHOR INFORMATION

Corresponding Author

Sebastian Dierickx – Institute for Applied Materials (IAM-ET), Karlsruhe Institute of Technology (KIT), D-76131

Karlsruhe, Germany; orcid.org/0000-0002-7936-854X;
Email: sebastian.dierickx.kit@gmail.com

Authors

Marius Müller – Institute for Applied Materials (IAM-ET), Karlsruhe Institute of Technology (KIT), D-76131 Karlsruhe, Germany; orcid.org/0000-0003-1557-0543

Johannes Schmieg – Institute for Applied Materials (IAM-ET) and Laboratory for Electron Microscopy (LEM), Karlsruhe Institute of Technology (KIT), D-76131 Karlsruhe, Germany

Jochen Joos – Institute for Applied Materials (IAM-ET), Karlsruhe Institute of Technology (KIT), D-76131 Karlsruhe, Germany

André Weber – Institute for Applied Materials (IAM-ET), Karlsruhe Institute of Technology (KIT), D-76131 Karlsruhe, Germany

Dagmar Gerthsen – Laboratory for Electron Microscopy (LEM), Karlsruhe Institute of Technology (KIT), D-76131 Karlsruhe, Germany

Ellen Ivers-Tiffée – Institute for Applied Materials (IAM-ET), Karlsruhe Institute of Technology (KIT), D-76131 Karlsruhe, Germany

Complete contact information is available at:

<https://pubs.acs.org/10.1021/acsami.1c25257>

Notes

The authors declare no competing financial interest.

■ ACKNOWLEDGMENTS

The authors gratefully acknowledge funding from the Federal Ministry of Education and Research within the FESTBATT project (BMBF 03XP0176A), InCa project (BMBF 03XP0228A), and the Deutsche Forschungsgemeinschaft (DFG) in the framework of the research training group SiMET (281041241/GRK2218).

■ REFERENCES

- (1) Zhu, Y.; He, X.; Mo, Y. Origin of Outstanding Stability in the Lithium Solid Electrolyte Materials: Insights from Thermodynamic Analyses Based on First-Principles Calculations. *ACS Appl. Mater. Interfaces* **2015**, *7*, 23685–23693.
- (2) Richards, W. D.; Miara, L. J.; Wang, Y.; Kim, J. C.; Ceder, G. Interface Stability in Solid-State Batteries. *Chem. Mater.* **2016**, *28*, 266–273.
- (3) Sharafi, A.; Yu, S.; Naguib, M.; Lee, M.; Ma, C.; Meyer, H. M.; Nanda, J.; Chi, M.; Siegel, D. J.; Sakamoto, J. Impact of Air Exposure and Surface Chemistry on $\text{Li-Li}_7\text{La}_3\text{Zr}_2\text{O}_{12}$ Interfacial Resistance. *J. Mater. Chem. A* **2017**, *5*, 13475–13487.
- (4) Sharafi, A.; Kazyak, E.; Davis, A. L.; Yu, S.; Thompson, T.; Siegel, D. J.; Dasgupta, N. P.; Sakamoto, J. Surface Chemistry Mechanism of Ultra-Low Interfacial Resistance in the Solid-State Electrolyte $\text{Li}_7\text{La}_3\text{Zr}_2\text{O}_{12}$. *Chem. Mater.* **2017**, *29*, 7961–7968.
- (5) Krauskopf, T.; Hartmann, H.; Zeier, W. G.; Janek, J. Toward a Fundamental Understanding of the Lithium Metal Anode in Solid-State Batteries - An Electrochemo-Mechanical Study on the Garnet-Type Solid Electrolyte $\text{Li}_{6.25}\text{Al}_{0.25}\text{La}_3\text{Zr}_2\text{O}_{12}$. *ACS Appl. Mater. Interfaces* **2019**, *11*, 14463–14477.
- (6) McOwen, D. W.; Xu, S.; Gong, Y.; Wen, Y.; Godbey, G. L.; Gritton, J. E.; Hamann, T. R.; Dai, J.; Hitz, G. T.; Hu, L.; Wachsman, E. D. 3D-Printing Electrolytes for Solid-State Batteries. *Adv. Mater.* **2018**, *30*, No. 1707132.
- (7) Lu, Y.; Huang, X.; Ruan, Y.; Wang, Q.; Kun, R.; Yang, J.; Wen, Z. An In Situ Element Permeation Constructed High Endurance Li-LLZO Interface at High Current Densities. *J. Mater. Chem. A* **2018**, *6*, 18853–18858.

- (8) Zhong, Y.; Xie, Y.; Hwang, S.; Wang, Q.; Cha, J. J.; Su, D.; Wang, H. A Highly Efficient All-Solid-State Lithium/Electrolyte Interface Induced by an Energetic Reaction. *Angew. Chem., Int. Ed.* **2020**, *59*, 14003–14008.
- (9) Han, X.; Gong, Y.; Fu, K.; He, X.; Hitz, G. T.; Dai, J.; Pearse, A.; Liu, B.; Wang, H.; Rubloff, G.; Mo, Y.; Thangadurai, V.; Wachsman, E. D.; Hu, L. Negating Interfacial Impedance in Garnet-Based Solid-State Li Metal Batteries. *Nat. Mater.* **2017**, *16*, 572–579.
- (10) Fu, K. K.; Gong, Y.; Liu, B.; Zhu, Y.; Xu, S.; Yao, Y.; Luo, W.; Wang, C.; Lacey, S. D.; Dai, J.; Chen, Y.; Mo, Y.; Wachsman, E.; Hu, L. Toward Garnet Electrolyte-Based Li Metal Batteries: An Ultrathin, Highly Effective, Artificial Solid-State Electrolyte/Metallic Li Interface. *Sci. Adv.* **2017**, *3*, No. e1601659.
- (11) Tsai, C. L.; Roddatis, V.; Chandran, C. V.; Ma, Q.; Uhlenbruck, S.; Bram, M.; Heitjans, P.; Guillon, O. Li₇La₃Zr₂O₁₂ Interface Modification for Li Dendrite Prevention. *ACS Appl. Mater. Interfaces* **2016**, *8*, 10617–10626.
- (12) Luo, W.; Gong, Y.; Zhu, Y.; Li, Y.; Yao, Y.; Zhang, Y.; Fu, K. K.; Pastel, G.; Lin, C. F.; Mo, Y.; Wachsman, E. D.; Hu, L. Reducing Interfacial Resistance between Garnet-Structured Solid-State Electrolyte and Li-Metal Anode by a Germanium Layer. *Adv. Mater.* **2017**, *29*, No. 1606042.
- (13) Wang, C.; Gong, Y.; Liu, B.; Fu, K.; Yao, Y.; Hitz, E.; Li, Y.; Dai, J.; Xu, S.; Luo, W.; Wachsman, E. D.; Hu, L. Conformal, Nanoscale ZnO Surface Modification of Garnet-Based Solid-State Electrolyte for Lithium Metal Anodes. *Nano Lett.* **2017**, *17*, 565–571.
- (14) Liu, K.; Li, Y.; Zhang, R.; Wu, M.; Huang, B.; Zhao, T. Facile Surface Modification Method To Achieve an Ultralow Interfacial Resistance in Garnet-Based Li Metal Batteries. *ACS Appl. Energy Mater.* **2019**, *2*, 6332–6340.
- (15) Krauskopf, T.; Mogwitz, B.; Hartmann, H.; Singh, D. K.; Zeier, W. G.; Janek, J. The Fast Charge Transfer Kinetics of the Lithium Metal Anode on the Garnet-Type Solid Electrolyte Li_{6.25}Al_{0.25}La₃Zr₂O₁₂. *Adv. Energy Mater.* **2020**, *10*, No. 2000945.
- (16) Santhosha, A. L.; Medenbach, L.; Buchheim, J. R.; Adelhelm, P. The Indium–Lithium Electrode in Solid-State Lithium-Ion Batteries: Phase Formation, Redox Potentials, and Interface Stability. *Batteries Supercaps* **2019**, *2*, 524–529.
- (17) Luo, S.; Wang, Z.; Li, X.; Liu, X.; Wang, H.; Ma, W.; Zhang, L.; Zhu, L.; Zhang, X. Growth of Lithium-Indium Dendrites in All-Solid-State Lithium-Based Batteries with Sulfide Electrolytes. *Nat. Commun.* **2021**, *12*, No. 6968.
- (18) Lou, J.; Wang, G.; Xia, Y.; Liang, C.; Huang, H.; Gan, Y.; Tao, X.; Zhang, J.; Zhang, W. Achieving Efficient and Stable Interface between Metallic Lithium and Garnet-Type Solid Electrolyte through a Thin Indium Tin Oxide Interlayer. *J. Power Sources* **2020**, *448*, No. 227440.
- (19) Flatscher, F.; Philipp, M.; Ganschow, S.; Wilkening, H. M. R.; Rettenwander, D. The Natural Critical Current Density Limit for Li₇La₃Zr₂O₁₂ Garnets. *J. Mater. Chem. A* **2020**, *8*, 15782–15788.
- (20) Tsai, C.-L.; Roddatis, V.; Chandran, C. V.; Ma, Q.; Uhlenbruck, S.; Bram, M.; Heitjans, P.; Guillon, O. Li₇La₃Zr₂O₁₂ Interface Modification for Li Dendrite Prevention. *ACS Appl. Mater. Interfaces* **2016**, *8*, 10617–10626.
- (21) Fu, K. K.; Gong, Y.; Fu, Z.; Xie, H.; Yao, Y.; Liu, B.; Carter, M.; Wachsman, E.; Hu, L. Transient Behavior of the Metal Interface in Lithium Metal–Garnet Batteries. *Angew. Chem., Int. Ed.* **2017**, *56*, 14942–14947.
- (22) Randau, S.; Weber, D. A.; Kötz, O.; Koerver, R.; Braun, P.; Weber, A.; Ivers-Tiffée, E.; Adermann, T.; Kulisch, J.; Zeier, W. G.; Richter, F. H.; Janek, J. Benchmarking the Performance of All-Solid-State Lithium Batteries. *Nat. Energy* **2020**, *5*, 259–270.
- (23) Wang, M.; Wolfenstine, J. B.; Sakamoto, J. Temperature Dependent Flux Balance of the Li/Li₇La₃Zr₂O₁₂ Interface. *Electrochim. Acta* **2019**, *296*, 842–847.
- (24) Koshikawa, H.; Matsuda, S.; Kamiya, K.; Miyayama, M.; Kubo, Y.; Uosaki, K.; Hashimoto, K.; Nakanishi, S. Dynamic Changes in Charge-Transfer Resistance at Li Metal/Li₇La₃Zr₂O₁₂ Interfaces during Electrochemical Li Dissolution/Deposition Cycles. *J. Power Sources* **2018**, *376*, 147–151.
- (25) Aguesse, F.; Manalastas, W.; Buannic, L.; Del Amo, J. M. L.; Singh, G.; Llordés, A.; Kilner, J. Investigating the Dendritic Growth during Full Cell Cycling of Garnet Electrolyte in Direct Contact with Li Metal. *ACS Appl. Mater. Interfaces* **2017**, *9*, 3808–3816.
- (26) Ren, Y.; Shen, Y.; Lin, Y.; Nan, C. W. Direct Observation of Lithium Dendrites inside Garnet-Type Lithium-Ion Solid Electrolyte. *Electrochem. Commun.* **2015**, *57*, 27–30.
- (27) Swamy, T.; Park, R.; Sheldon, B. W.; Rettenwander, D.; Porz, L.; Berendts, S.; Uecker, R.; Craig Carter, W.; Chiang, Y. M. Lithium Metal Penetration Induced by Electrodeposition through Solid Electrolytes: Example in Single-Crystal Li₆La₃Zr₂O₁₂ Garnet. 2018, arXiv:1808.02105. arXiv.org e-Print archive. <https://arxiv.org/abs/1808.02105>.
- (28) Porz, L.; Swamy, T.; Sheldon, B. W.; Rettenwander, D.; Frömling, T.; Thaman, H. L.; Berendts, S.; Uecker, R.; Carter, W. C.; Chiang, Y. M. Mechanism of Lithium Metal Penetration through Inorganic Solid Electrolytes. *Adv. Energy Mater.* **2017**, *7*, No. 1701003.
- (29) Cheng, E. J.; Sharafi, A.; Sakamoto, J. Intergranular Li Metal Propagation through Polycrystalline Li_{6.25}Al_{0.25}La₃Zr₂O₁₂ Ceramic Electrolyte. *Electrochim. Acta* **2017**, *223*, 85–91.
- (30) Krauskopf, T.; Richter, F. H.; Zeier, W. G.; Janek, J. Physicochemical Concepts of the Lithium Metal Anode in Solid-State Batteries. *Chem. Rev.* **2020**, *120*, 7745–7794.
- (31) Cao, D.; Sun, X.; Li, Q.; Natan, A.; Xiang, P.; Zhu, H. Lithium Dendrite in All-Solid-State Batteries: Growth Mechanisms, Suppression Strategies, and Characterizations. *Matter* **2020**, *3*, 57–94.
- (32) Kazyak, E.; Garcia-Mendez, R.; LePage, W. S.; Sharafi, A.; Davis, A. L.; Sanchez, A. J.; Chen, K. H.; Haslam, C.; Sakamoto, J.; Dasgupta, N. P. Li Penetration in Ceramic Solid Electrolytes: Operando Microscopy Analysis of Morphology, Propagation, and Reversibility. *Matter* **2020**, *2*, 1025–1048.
- (33) Illig, J.; Schmidt, J. P.; Weiss, M.; Weber, A.; Ivers-Tiffée, E. Understanding the Impedance Spectrum of 18650 LiFePO₄-Cells. *J. Power Sources* **2013**, *239*, 670–679.
- (34) Uhlmann, C.; Illig, J.; Ender, M.; Schuster, R.; Ivers-Tiffée, E. In Situ Detection of Lithium Metal Plating on Graphite in Experimental Cells. *J. Power Sources* **2015**, *279*, 428–438.
- (35) Boukamp, B. A. A Linear Kronig-Kramers Transform Test for Immittance Data Validation. *J. Electrochem. Soc.* **1995**, *142*, 1885.
- (36) Schönleber, M.; Klotz, D.; Ivers-Tiffée, D.; Kramers-Kronig, E. Validity Test Lin-KK for Impedance Spectra.
- (37) Schönleber, M.; Ivers-Tiffée, E. Approximability of Impedance Spectra by RC Elements and Implications for Impedance Analysis. *Electrochem. Commun.* **2015**, *58*, 15–19.
- (38) Braun, P.; Uhlmann, C.; Weber, A.; Störmer, H.; Gerthsen, D.; Ivers-Tiffée, E. Separation of the Bulk and Grain Boundary Contributions to the Total Conductivity of Solid Lithium-Ion Conducting Electrolytes. *J. Electroceramics* **2017**, *38*, 157–167.
- (39) Schichlein, H.; Müller, A. C.; Voigts, M.; Krügel, A.; Ivers-Tiffée, E. Deconvolution of Electrochemical Impedance Spectra for the Identification of Electrode Reaction Mechanisms in Solid Oxide Fuel Cells. *J. Appl. Electrochem* **2002**, *32*, 875–882.
- (40) Dierickx, S.; Weber, A.; Ivers-Tiffée, E. How the Distribution of Relaxation Times Enhances Complex Equivalent Circuit Models for Fuel Cells. *Electrochimica Acta* **2020**, *355*, No. 136764.
- (41) Mertens, A.; Yu, S.; Schön, N.; Gunduz, D. C.; Tempel, H.; Schierholz, R.; Hausen, F.; Kungl, H.; Granwehr, J.; Eichel, R. A. Superionic Bulk Conductivity in Li_{1.3}Al_{0.3}Ti_{1.7}(PO₄)₃ Solid Electrolyte. *Solid State Ionics* **2017**, *309*, 180–186.
- (42) Schmidt, J. P.; Berg, P.; Schönleber, M.; Weber, A.; Ivers-Tiffée, E. The Distribution of Relaxation Times as Basis for Generalized Time-Domain Models for Li-Ion Batteries. *J. Power Sources* **2013**, *221*, 70–77.
- (43) Shen, F.; Dixit, M. B.; Xiao, X.; Hatzell, K. B. Effect of Pore Connectivity on Li Dendrite Propagation within LLZO Electrolytes Observed with Synchrotron X-Ray Tomography. *ACS Energy Lett.* **2018**, *3*, 1056–1061.
- (44) Songster, J.; Pelton, A. The In-Li (Indium-Lithium) System. *J. Phase Equilibria* **1991**, *12*, 37–41.

(45) He, M.; Cui, Z.; Chen, C.; Li, Y.; Guo, X. Formation of Self-Limited, Stable and Conductive Interfaces between Garnet Electrolytes and Lithium Anodes for Reversible Lithium Cycling in Solid-State Batteries. *J. Mater. Chem. A* **2018**, *6*, 11463–11470.

(46) Wang, Y.; Lai, W. High Ionic Conductivity Lithium Garnet Oxides of Li₇-XLa₃Zr₂-XTa₁XO₁₂ Compositions. *Electrochem. Solid-State Lett.* **2012**, *15*, No. A68.

(47) Buschmann, H.; Berendts, S.; Mogwitz, B.; Janek, J. Lithium Metal Electrode Kinetics and Ionic Conductivity of the Solid Lithium Ion Conductors “Li₇La₃Zr₂O₁₂” and Li₇-XLa₃Zr₂-XTa₁XO₁₂ with Garnet-Type Structure. *J. Power Sources* **2012**, *206*, 236–244.

(48) Tenhaeff, W. E.; Rangasamy, E.; Wang, Y.; Sokolov, A. P.; Wolfenstine, J.; Sakamoto, J.; Dudney, N. J. Resolving the Grain Boundary and Lattice Impedance of Hot-Pressed Li₇La₃Zr₂O₁₂ Garnet Electrolytes. *ChemElectroChem* **2014**, *1*, 375–378.

(49) Yu, S.; Siegel, D. J. Grain Boundary Contributions to Li-Ion Transport in the Solid Electrolyte Li₇La₃Zr₂O₁₂ (LLZO). *Chem. Mater.* **2017**, *29*, 9639–9647.

(50) Lu, Y.; Zhao, C. Z.; Yuan, H.; Cheng, X. B.; Huang, J. Q.; Zhang, Q. Critical Current Density in Solid-State Lithium Metal Batteries: Mechanism, Influences, and Strategies. *Adv. Funct. Mater.* **2021**, *31*, No. 2009925.

(51) Kim, J.-S.; Lee, D. C.; Lee, J. J.; Kim, C. W. Optimization for Maximum Specific Energy Density of a Lithium-Ion Battery Using Progressive Quadratic Response Surface Method and Design of Experiments. *Sci. Rep.* **2020**, *10*, No. 15586.

(52) Yoo, H. I.; Lee, J. H.; Martin, M.; Janek, J.; Schmalzried, H. Experimental Evidence of the Interference between Ionic and Electronic Flows in an Oxide with Prevailing Electronic Conduction. *Solid State Ionics* **1994**, *67*, 317–322.

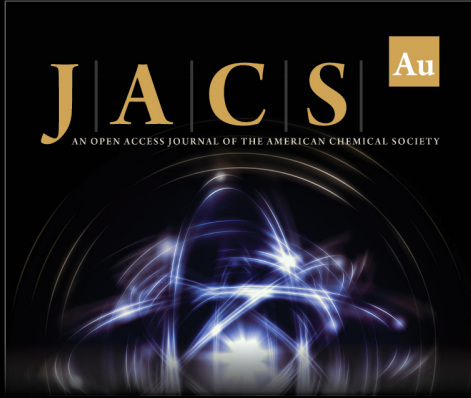
(53) Albertus, P.; Babinec, S.; Litzelman, S.; Newman, A. Status and Challenges in Enabling the Lithium Metal Electrode for High-Energy and Low-Cost Rechargeable Batteries. *Nat. Energy* **2018**, *3*, 16–21.

(54) Dong, Y.; Zhang, Z.; Alvarez, A.; Chen, I. W. Potential Jumps at Transport Bottlenecks Cause Instability of Nominally Ionic Solid Electrolytes in Electrochemical Cells. *Acta Mater.* **2020**, *199*, 264–277.

(55) Han, F.; Westover, A. S.; Yue, J.; Fan, X.; Wang, F.; Chi, M.; Leonard, D. N.; Dudney, N. J.; Wang, H.; Wang, C. High Electronic Conductivity as the Origin of Lithium Dendrite Formation within Solid Electrolytes. *Nat. Energy* **2019**, *4*, 187–196.


(56) Famprakis, T.; Canepa, P.; Dawson, J. A.; Islam, M. S.; Masquelier, C. Fundamentals of Inorganic Solid-State Electrolytes for Batteries. *Nat. Mater.* **2019**, *18*, 1278–1291.


(57) Wolfenstine, J.; Allen, J. L.; Sakamoto, J.; Siegel, D. J.; Choe, H. Mechanical Behavior of Li-Ion-Conducting Crystalline Oxide-Based Solid Electrolytes: A Brief Review. *Ionics* **2018**, *24*, 1271–1276.



JACS Au
AN OPEN ACCESS JOURNAL OF THE AMERICAN CHEMICAL SOCIETY

Editor-in-Chief
Prof. Christopher W. Jones
Georgia Institute of Technology, USA

Open for Submissions 

pubs.acs.org/jacsau  ACS Publications
Most Trusted. Most Cited. Most Read.